# Nickel-Rich Layered Microspheres Cathodes: Lithium/Nickel Disordering and Electrochemical Performance

Chaochao Fu,[†] Guangshe Li,[‡] Dong Luo,[†] Qi Li,[‡] Jianming Fan,[†] and Liping Li*,[†]

[†]Key Lab of Optoelectronic Materials Chemistry and Physics, Fujian Institute of Research on the Structure of Matter, and [‡]State Key Laboratory of Structural Chemistry, Fujian Institute of Research on the Structure of Matter, University of Chinese Academy of Sciences, Fuzhou 350002, P. R. China

ⓢ *Supporting Information*
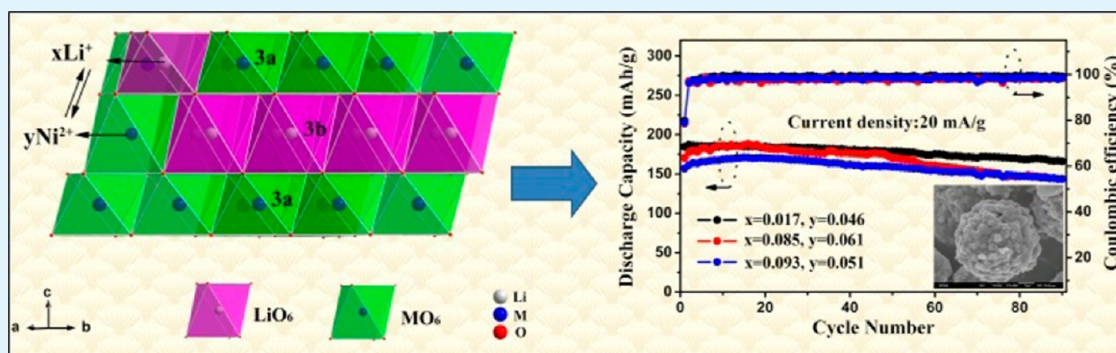
ABSTRACT: Nickel-rich layered metal oxide materials are prospective cathode materials for lithium ion batteries due to the relatively higher capacity and lower cost than $LiCoO_2$. Nevertheless, the disordered arrangement of Li^+/Ni^{2+} in local regions of these materials and its impact on electrochemistry performance are not well understood, especially for $LiNi_{1-x-y}Co_xMn_yO_2$ ($1-x-y > 0.5$) cathodes, which challenge one's ability in finding more superior cathode materials for advanced lithium-ion batteries. In this work, Ni–Co–Mn-based spherical precursors were first obtained by a solvothermal method through handily utilizing the redox reaction of nitrate and ethanol. Subsequent sintering of the precursors with given amount of lithium source (Li-excess of 5, 10, and 15 mol %) yields $LiNi_{0.7}Co_{0.15}Mn_{0.15}O_2$ microspheres with different extents of Li^+/Ni^{2+} disordering. With the determination of the amounts of Li^+ ions in transition metal layer and Ni^{2+} ions in Li layer using structural refinement, the impact of Li^+/Ni^{2+} ions disordering on the crystal structure, valence state of nickel ions, and electrochemical performance were investigated in detailed. It is clearly demonstrated that with increasing the amount of lithium source, lattice parameters (*a* and *c*) and interslab space thickness of unit cell decrease, and more Li^+ ions incorporated into the 3a site of transition metal layer which leads to an increase of Ni^{3+} content in $LiNi_{0.7}Co_{0.15}Mn_{0.15}O_2$ as confirmed by X-ray photoelectron spectroscopy and a redox titration. Moreover, the electrochemical performance for as-prepared $LiNi_{0.7}Co_{0.15}Mn_{0.15}O_2$ microspheres exhibited a trend of deterioration due to the changes of crystal structure from Li^+/Ni^{2+} mixing. The preparation method and the impacts of Li^+/Ni^{2+} ions disordering reported herein for the nickel-rich layered $LiNi_{0.7}Co_{0.15}Mn_{0.15}O_2$ microspheres may provide hints for obtaining a broad class of nickel-rich layered metal oxide microspheres with superior electrochemical performance.

KEYWORDS: *nickel-rich, cathode, $LiNi_{0.7}Co_{0.15}Mn_{0.15}O_2$ microspheres, lithium/nickel disordering, Li-ion batteries*

1. INTRODUCTION

Rechargeable lithium-ion batteries, a rapidly developing technology in energy storage and conversion, are the most important power sources for portable electronic devices and are the most promising power supplies for electric vehicles because of their high energy density, long cycling life, and fast charging/discharging rate.[1–5] As a cathode material, $LiCoO_2$ has dominated the commercialized lithium-ion batteries in the past decades. Nevertheless, because of the limitation of its structure stability, $LiCoO_2$ delivers a low reversible capacity of 140 mAh/g, only half of the theoretical capacity,[6–9] which imposes a major obstacle for applications in large capacity lithium-ion batteries like those for electric vehicles. Besides this, the high cost and toxicity of cobalt are other hindrances for

further applications. Therefore, it is very important, but highly challenging, to develop alternative cathode materials of lower cost and higher capacity.

$LiNiO_2$ seems to be a potential candidate due to its lower cost and higher capacity (>200 mAh/g).[10–13] Unfortunately, extra nickel ions would occupy the sites in Li layer with a formula of $(Li_{1-x}Ni_x)NiO_2$,[14–17] which result in a deterioration of electrochemical performance. Comparatively, nickel-rich layered $LiNi_{1-x-y}Co_xMn_yO_2$ ($1-x-y > 0.5$) materials are promising because of their higher capacity, relatively lower
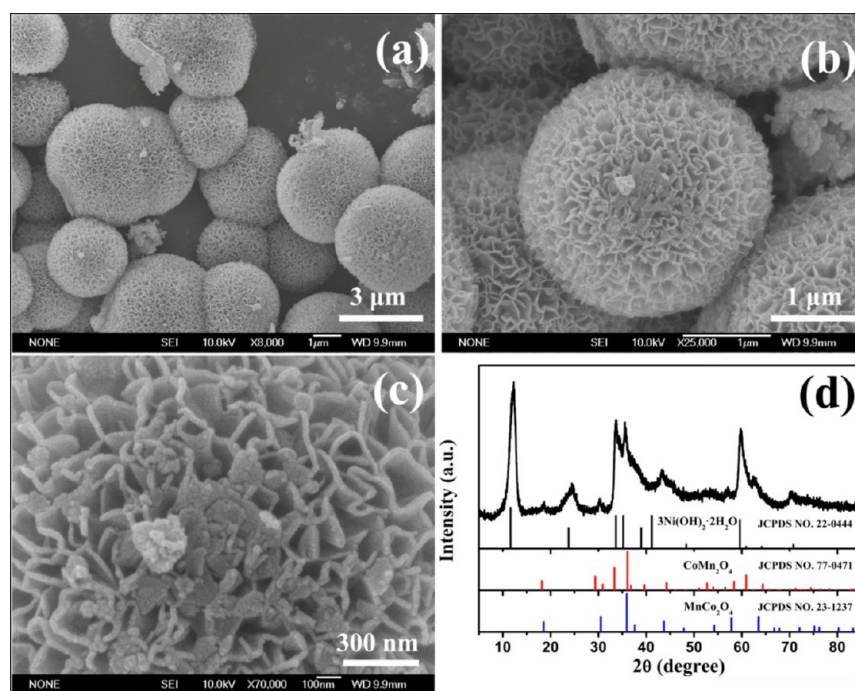
Figure 1. (a−c) Low-magnification and high-magnification SEM images and (d) XRD patterns of precursors prepared by solvothermal method.

cost, superior cycling stability, and better environmental benignancy. Even so, these nickel-rich layered materials still suffer from the inevitable, but also poorly understood impacts of disordered distribution for Li^+ and Ni^{2+} ions, because the similar ionic sizes (i.e., 0.76 Å for Li^+ vs 0.69 Å for Ni^{2+})[11,18] allow a disordered arrangement between transition metal layer (3a site) and Li layer (3b site), as widely indicated in a series of layered $LiNi_{1−x−y}Co_xMn_yO_2$ materials, particularly in the compounds with larger content of nickel ions. The presence of Ni^{2+} in Li layer would block the lithium-ions diffusion and induce a decrease in reversible capacity. Lithium ions located in transition metal layers are very difficult to be deintercalated from the crystal lattice, which results in a poor electrochemical performance.[14−17,19] One may imagine that if the impacts of Li^+/Ni^{2+} mixing on the crystal structure and electrochemical performance could be well uncovered for nickel-rich layered $LiNi_{1−x−y}Co_xMn_yO_2$ ($1−x−y > 0.5$), it is highly possible to find more superior cathode materials for advanced lithium-ion batteries.

In this work, nickel-rich layered $LiNi_{1−x−y}Co_xMn_yO_2$ at $x = y = 0.15$ material was selected as a typical compound to study. First, $LiNi_{0.7}Co_{0.15}Mn_{0.15}O_2$ microspheres were prepared by two-step processes that involve the initial formation of Ni−Co−Mn-based spherical precursors and the subsequent sintering. The resulted samples were tailored to show different disordered extents of Li^+/Ni^{2+}, when tuning the amount of lithium source (Li-excess of 5, 10, and 15 mol %). Eventually, the amounts of Li^+ ions in transition metal layer and Ni^{2+} ions in Li layer were determined by structural refinements, clearly demonstrating the impacts of Li^+/Ni^{2+} disordering on crystal structure, valence state of nickel ions, and electrochemical performance.

2. EXPERIMENTAL SECTION

2.1. Sample Synthesis. *Ni−Co−Mn-Based Spherical Precursors.* The synthetic procedure can be described as follows: First, 14 mmol of $Ni(NO_3)_2 \cdot 6H_2O$, 3 mmol of $Co(NO_3)_2 \cdot 6H_2O$, and 3 mmol of $Mn(NO_3)_2$ (50 wt % water solution) were dissolved in 50 mL of absolute ethanol at room temperature to form a clear solution. The resulted transparent solution was transferred into a 100 mL autoclave and maintained at 160 °C for 12 h. After reactions, the precipitate was collected and washed with absolute ethanol several times. After drying at 80 °C for 8 h in air, the precursor was obtained.

$LiNi_{0.7}Co_{0.15}Mn_{0.15}O_2$ Microspheres. The synthetic procedure can be described briefly as follows. Ni−Co−Mn-based precursors (containing 20 mmol metal ions) were thoroughly mixed with 21 (Li excess of 5 mol %), 22 (Li excess of 10 mol %), or 23 (Li excess of 15 mol %) mmol of $LiNO_3$ and $LiOH \cdot H_2O$ (at a molar ratio of $LiNO_3$ to LiOH at 61:39) in 20 mL of absolute ethanol, respectively. The ethanol was evaporated slowly at 80 °C under stirring. The mixture was ground manually for 10 min and then sintered at 480 and 750 °C in an O_2 flow for 5 and 16 h, respectively. The final products with Li excess of 5, 10, and 15 mol % were named as E5, E10, and E15, respectively.

2.2. Materials Characterization. Phase structures of the samples were characterized by powder X-ray diffraction (XRD) (Cu Kα, λ = 1.5418 Å) on a Rigaku Miniflex apparatus. The morphology of the samples was observed by field-emission scanning electron microscopy (SEM) (JEOL, Model JEM-2010) and transmission electron microscopy (TEM) (JEOL, Model JEM-2010). The chemical compositions of the samples were analyzed by inductive coupled plasma atomic emission spectrometry (ICP-AES). The valence states of Ni, Co, and Mn ions were examined by X-ray photoelectron spectroscopy (XPS) recorded on ESCA-LAB MKII apparatus with a monochromatic Al Kα X-ray source and titration with excess sodium oxalate solution (0.075 M) using standard $KMnO_4$ solution (0.02 M), respectively. During XPS measurements, the base pressure of sample chamber was kept below 3.0×10^{-10} Mbar. Emission lines were calibrated with C 1s signal at 284.6 eV. In addition, the amount of Ni^{3+} in the samples is calculated by the peak area ratio of $Ni^{3+}/(Ni^{2+}+Ni^{3+})$ and the experimental results of the redox titration are given through three timed tests.
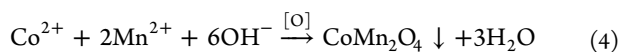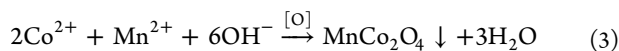
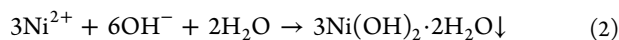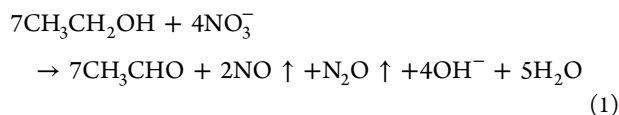**2.3. Electrochemical Measurements.** Electrochemical behaviors of the samples were examined using CR-2025-type coin cell. The cells were composed of a cathode and a lithium foil anode separated by a polymer separator (Celgard 2500). The cathode film was fabricated from a mixture of synthesized samples, carbon black (Super P Li, Timcal) and binder (polyvinylidene fluoride (PVDF), Alfa Aesar) in a

weight ratio of 8:1:1 using *N*-methylpyrrolidinone (NMP, Alfa Aesar) as solution. The resulting slurry was coated on Al foil by a doctor blade technique and dried at 100 °C for 10 h. The cells were assembled in an argon-filled glovebox (H_2O and $O_2 < 1$ ppm) using 1 M $LiPF_6$ in EC:EMC:DMC (1:1:1 in volume) as the electrolyte. The cells were charged galvanostatically at different current densities of 20, 50, 100, 200, and 400 mA/g to 4.3 V, held at 4.3 V until the current decreased to 20 mA/g, and then discharged galvanostatically at corresponding current densities of 20, 50, 100, 200, and 400 mA/g to 2.8 V using a battery cycler (Neware Test System) at room temperature. The electrochemical impedance spectroscopy (EIS) was measured using an electrochemical workstation (CHI660C) and the applied frequency is from 100 kHz to 10 mHz.

3. RESULTS AND DISCUSSION

3.1. Formation of $LiNi_{0.7}Co_{0.15}Mn_{0.15}O_2$ Microspheres.
Ni−Co−Mn-based spherical precursors for Li-$Ni_{0.7}Co_{0.15}Mn_{0.15}O_2$ microspheres were first synthesized under solvothermal condition. The morphology of the precursors was investigated by SEM. As shown in Figure 1a, b, the as-prepared precursors were composed of flowerlike microspheres with a dimension around 2−6 μm. All these microspheres were assembled by nanosheets in Figure 1c. Concerning the phase structures of the precursor, as indicated in Figure 1d, all diffraction peaks were divided into three sets of data, which correspond to $3Ni(OH)_2 \cdot 2H_2O$ (JCPDS, No. 22−0444), $CoMn_2O_4$ (JCPDS, No. 77−0471), and $MnCo_2O_4$ (JCPDS, No. 23−1237), respectively. According to our previous reports,[20] the formation reactions of the precursor might be described in the following steps

$$7CH_3CH_2OH + 4NO_3^-$$
$$\rightarrow 7CH_3CHO + 2NO \uparrow + N_2O \uparrow + 4OH^- + 5H_2O \quad (1)$$

$$3Ni^{2+} + 6OH^- + 2H_2O \rightarrow 3Ni(OH)_2 \cdot 2H_2O\downarrow \quad (2)$$

$$2Co^{2+} + Mn^{2+} + 6OH^- \xrightarrow{[O]} MnCo_2O_4 \downarrow + 3H_2O \quad (3)$$

$$Co^{2+} + 2Mn^{2+} + 6OH^- \xrightarrow{[O]} CoMn_2O_4 \downarrow + 3H_2O \quad (4)$$

It should be mentioned that hydroxyl (OH^-) species originated from the reaction of ethanol and nitrate in the present synthesis lead to the precipitation of metal ion (Ni, Co, and Mn), as described in eqs 1−4.

To obtain nickel-rich layered microspheres Li-$Ni_{0.7}Co_{0.15}Mn_{0.15}O_2$, we further sintered Ni−Co−Mn-based spherical precursors with different amounts of lithium source (i.e., Li-excess of 5, 10, and 15 mol %) at 750 °C in an O_2 flow. Morphologies and microstructures of the samples E5, E10, and E15 were characterized by SEM and TEM. As indicated in Figure 2, all three sintered samples with different amounts of lithium source had similar microspherical morphology as assembled by particles with size distributed in a range from 100 to 500 nm, which inherited the morphology of Ni−Co−Mn-based spherical precursors.

More detailed morphological and structure features of these samples were further studied by TEM, as shown in Figure 3. For sample E5, the particle is composed of solid microspheres with a diameter >1 μm (Figure 3a$_1$, a$_2$). A high-resolution TEM image of the rectangular region in Figure 3a$_2$ is shown in Figure 3a$_3$. Both high-resolved lattice fringes and Fourier transform image shown in Figure 3a$_4$ for the chosen region in Figure 3a$_3$ indicate the appearance of two groups of vertical crystal planes
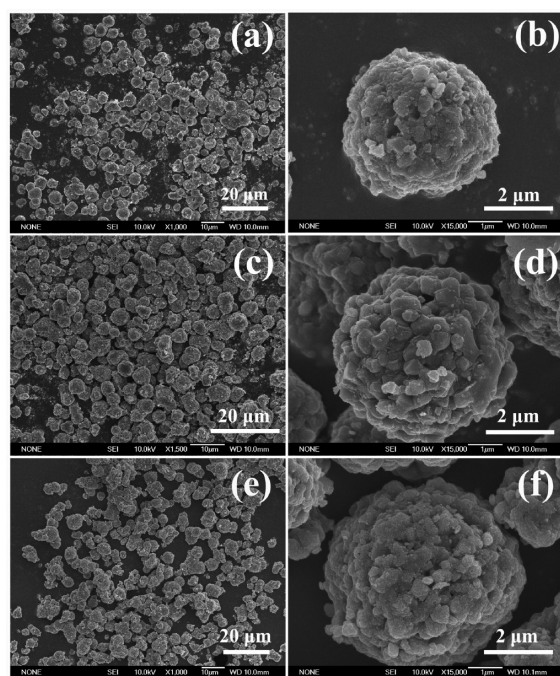

Figure 2. Low-magnification SEM images (left) and high-magnification SEM images (right) for $LiNi_{0.7}Co_{0.15}Mn_{0.15}O_2$ microspheres: (a, b) E5, (c, d) E10, and (e, f) E15.

with lattice spacings of 2.45 and 1.44 Å, which correspond to the planes (101) and ($\bar{1}20$), respectively. In addition, several sets of visible lattice fringes were observed by Fourier transform image, which could be assigned to the planes of (101), (021), ($\bar{1}20$), and ($\bar{2}21$), respectively (the incident beam parallel to crystal orientation of $[21\bar{2}]$). For sample E10, as indicated in Figure 3b$_1$, b$_2$, the microsphere is not hollow either. Figure 3b$_3$ shows that there are two groups of crystal planes with an angle of 119.5°, corresponding to the planes of ($\bar{1}01$) and ($1\bar{1}0$) with lattice spacing of 2.45 and 2.49 Å, respectively. Moreover, other two planes ($0\bar{1}1$) and ($2\bar{1}1$) were also observed by Fourier transform image in Figure 3b$_4$. Similar to samples E5 and E10, sample E15 is also shaped by solid assembled-microspheres (Figure 3c$_1$, c$_2$). Figure 3c$_3$, corresponding to region I in Figure 3c$_2$, exhibits a set of visible lattice fringes with a lattice spacing of 2.45 Å, which may be ascribed to the plane (101). Selected area electron diffraction (SAED) from region II in Figure 3c$_2$ is given in Figure 3c$_4$. There are three sets of crystal planes, which correspond to the planes (110), ($\bar{1}20$), and ($\bar{2}10$), respectively (the incident beam was parallel to [001]; that is, the exposed face was the plane (001)). As mentioned above, all samples E5, E10, and E15 have a similar morphology and inherit the morphology of Ni−Co−Mn-based spherical precursors.

Phase purity and chemical compositions of the samples E5, E10, and E15 were determined by XRD and ICP-AES. As indicated in Figure 4, all diffraction peaks for three samples can be well indexed in a hexagonal structure of α-$NaFeO_2$ type. Careful XRD data analyses showed that the intensity ratio of $I_{(003)}/I_{(104)}$ was 1.305 for E5, 1.138 for E10, and 1.135 for E15, indicating the indicating the least Li^+/Ni^{2+} disorder for E5. The results of ICP-AES indicated that the compositions of samples E5, E10, and E15 were $(Li_{0.971}Ni_{0.029})(Ni_{0.697}Co_{0.160}Mn_{0.143})O_2$, $Li(Li_{0.024}Ni_{0.680}Co_{0.157}Mn_{0.139})O_2$, and $Li(Li_{0.042}Ni_{0.669}Co_{0.151}Mn_{0.138})O_2$, respectively, approaching to the theoretical values of $LiNi_{0.7}Co_{0.15}Mn_{0.15}O_2$, as listed in
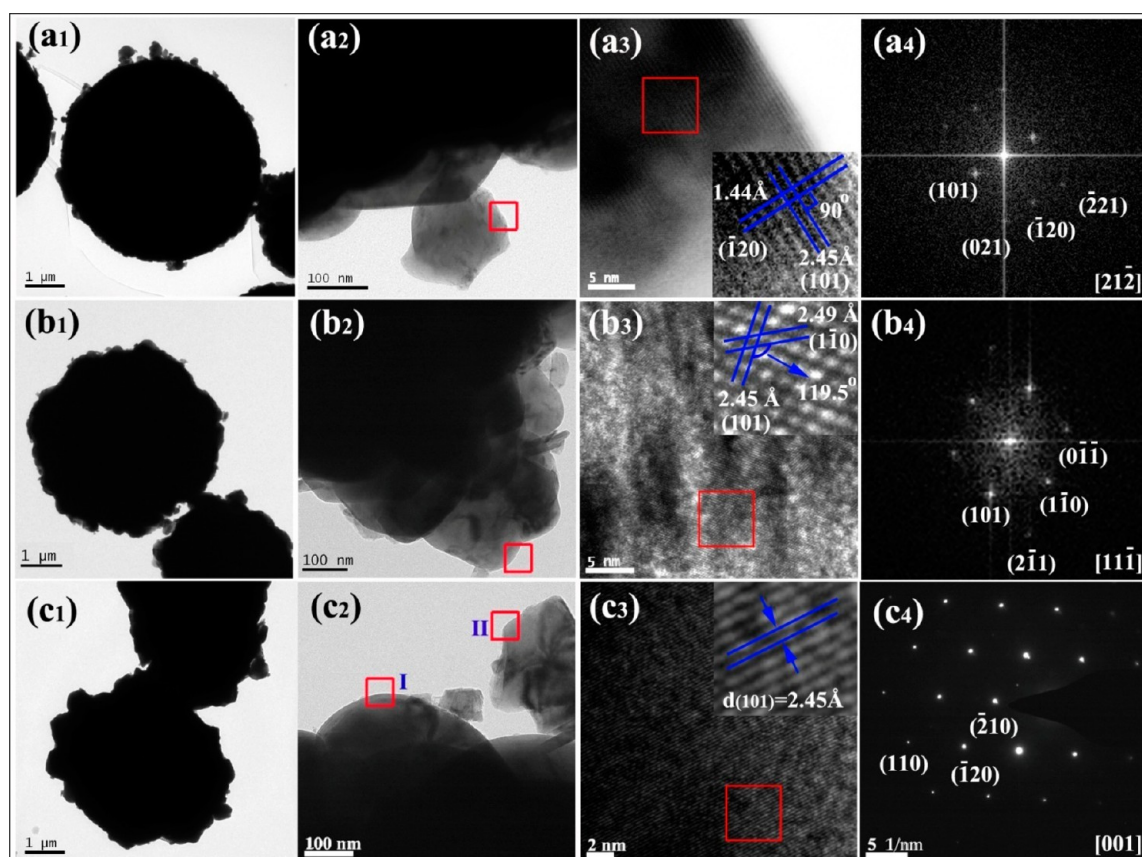
Figure 3. TEM, HRTEM, and FFT or SAED images of the samples, (a_1-a_4) E5, (b_1-b_4) E10, and (c_1-c_4) E15. HRTEM image in c_3 corresponds to region I, whereas SAED image in c_4 corresponds to region II.
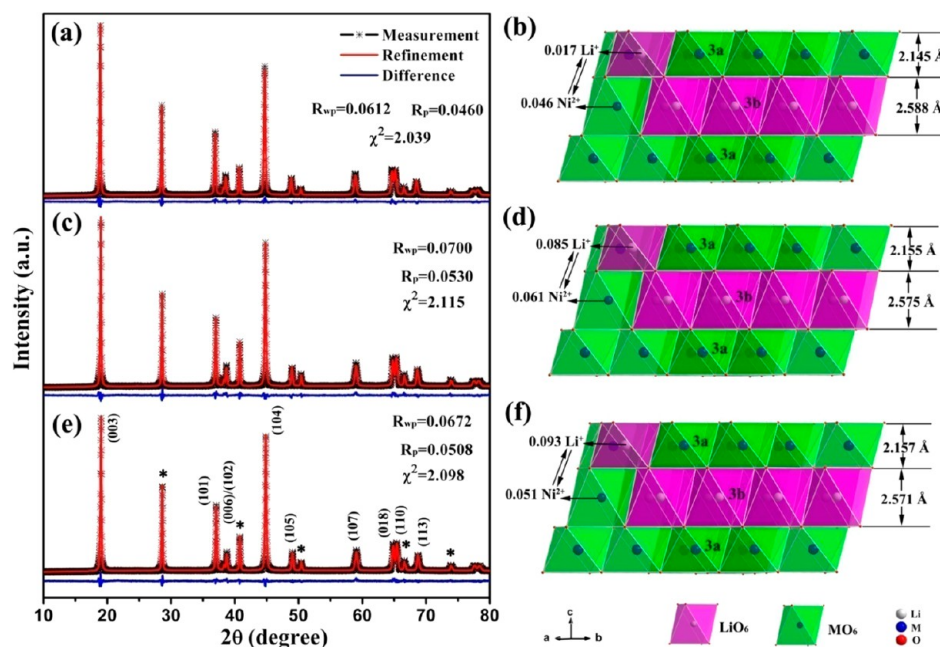

Figure 4. XRD patterns of the microspheres E5, E10, and E15. Black asterisk (*) denotes the internal standard of KCl.

Table 1. Obviously, with increasing the amount of lithium source, some of the lithium ions may occupy the sites of transition metal ions.

To reveal the detailed lattice parameters and lithium/nickel ion disorder, we refined XRD patterns of the samples by Rietveld method using GSAS software[21] based on the space group, $R\bar{3}m$, in which Li_1/Ni_2 was set at 3b site $(0, 0, 0.5)$, $Li_2/Ni_1/Co_1/Mn_1$ at 3a site $(0, 0, 0)$, and O at 6c site $(0, 0, z)$ with $z \approx 0.25$. The initial occupation parameters of all atoms were on the basis of formula $(Li_1Ni_2)_{3b}(Li_2Ni_1Co_1Mn_1)_{3a}O_2$, corresponding to the experimentally measured compositions from ICP mentioned above for samples. The occupation

Table 1. Molar Ratios of Li/Ni/Co/Mn from ICP-AES and Crystallographic Formulas Calculated from ICP and XRD Refinement for Samples E5, E10, and E15

sample	molar ratios of Li: Ni: Co: Mn	crystallographic formula from ICP	crystallographic formula from refinement	Ni^{2+} in Li layer	Li^+ in TM layer
E5	0.971:0.726:0.160:0.143	$(Li_{0.971}Ni_{0.029})(Ni_{0.697}Co_{0.160}Mn_{0.143})O_2$	$(Li^+_{0.954}Ni^{2+}_{0.046})_{3b}(Li^+_{0.017}Ni^{3+}_{0.525}Ni^{2+}_{0.155}Co^{3+}_{0.160}Mn^{4+}_{0.143})_{3a}O_2$	0.046(2)	0.017(2)
E10	1.024:0.680:0.157:0.139	$Li(Li_{0.024}Ni_{0.680}Co_{0.157}Mn_{0.139})O_2$	$(Li^+_{0.939}Ni^{2+}_{0.061})_{3b}(Li^+_{0.085}Ni^{3+}_{0.589}Ni^{2+}_{0.030}Co^{3+}_{0.157}Mn^{4+}_{0.139})_{3a}O_2$	0.061(4)	0.085(4)
E15	1.042:0.669:0.151:0.138	$Li(Li_{0.042}Ni_{0.669}Co_{0.151}Mn_{0.138})O_2$	$(Li^+_{0.949}Ni^{2+}_{0.051})_{3b}(Li^+_{0.093}Ni^{3+}_{0.615}Ni^{2+}_{0.003}Co^{3+}_{0.151}Mn^{4+}_{0.138})_{3a}O_2$	0.051(4)	0.093(4)
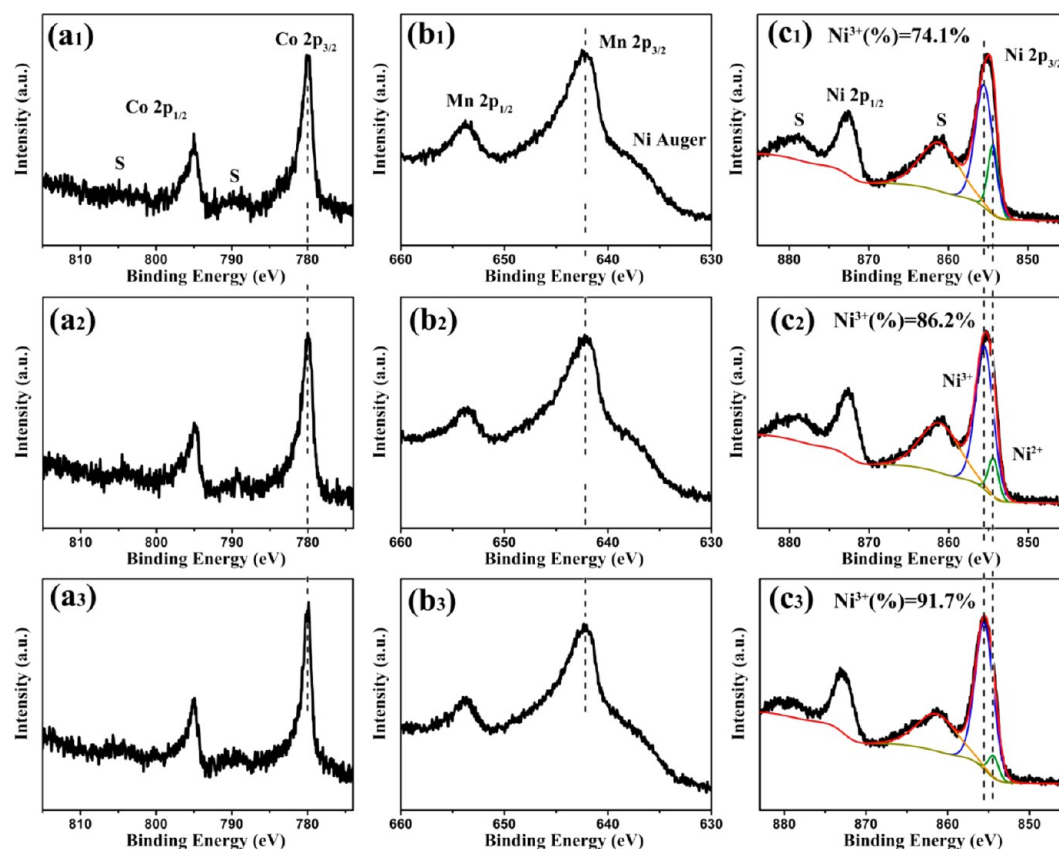
Figure 5. XPS data of (a_1-a_3) Co 2p, (b_1-b_3) Mn 2p, and (c_1-c_3) Ni 2p for samples E5, E10, and E15, respectively. Symbol "S" represents the satellite peaks for Co 2p levels or Ni 2p levels, respectively.

parameters of Co and Mn at 3a site were both fixed, and the sum of occupation parameters of Ni or Li being over two sites was also constrained at the experimentally measured compositions from ICP. Considering the previous experimental results on these materials,[22,23] manganese and cobalt ions were tetravalent and trivalent, respectively, whereas nickel ions were in a mixed valence state of divalent and trivalent, as confirmed by XPS measurements.

The results of XRD refinement for three samples of E5, E10, and E15 are given in Table 1. According to the calculated occupation parameters and valence state compensations, the crystallographic formulas and valence state of different elements for samples E5, E10, and E15 should be $(Li^+_{0.954}Ni^{2+}_{0.046})_{3b}(Li^+_{0.017}Ni^{3+}_{0.525}Ni^{2+}_{0.155}Co^{3+}_{0.160}Mn^{4+}_{0.143})_{3a}O_2$, $(Li^+_{0.939}Ni^{2+}_{0.061})_{3b}(Li^+_{0.085}Ni^{3+}_{0.589}Ni^{2+}_{0.030}Co^{3+}_{0.157}Mn^{4+}_{0.139})_{3a}O_2$, and $(Li^+_{0.949}Ni^{2+}_{0.051})_{3b}(Li^+_{0.093}Ni^{3+}_{0.615}Ni^{2+}_{0.003}Co^{3+}_{0.151}Mn^{4+}_{0.138})_{3a}O_2$, respectively. Obviously, with the increase in lithium-excess contents from 5 to 15 mol %, the amount of lithium occupied in transition metal layer (3a site) increases from 0.017 to 0.093, whereas the amount of Ni^{2+} occupied in the lithium layer (3b site) is 0.046, 0.061, and 0.051, respectively. It is well-documented that more cation exchange of Li^+ and Ni^{2+} would lead to the deterioration of electrochemical performance.[14−16,19] In this regard, both samples E10 and E15 with more amounts of cation disorder compared to sample E5 would have a relatively poor electrochemical performance. Moreover, the ratios of $Ni^{3+}/(Ni^{2+}+Ni^{3+})$ in samples E5, E10, and E15 are estimated to be 72.3, 86.6, and 91.9 mol %, respectively.

To further prove the rationality of the above results, we measured XPS spectra to examine the valence states of Ni, Co, and Mn ions of samples E5, E10, and E15. As shown in Figure $5a_1-a_3$, four signals that include two spin−orbit splitting peaks and two corresponding weak satellite peaks were detected for Co 2p core level. The most intense peak at 780 eV is due to the Co $2p_{3/2}$ main peak, and the peak at 795 eV is assigned to the Co $2p_{1/2}$ main peak. Moreover, all samples exhibited a sharp Co $2p_{3/2}$ peak: the full-width at half-maximum (FWHM) is only about 1.9 eV, and the binding energy difference between $2p_{3/2}$ and its satellite peak is about 9.6 eV. All these indicate that the

Table 2. Structure Parameters of Samples E5, E10, and E15 by Rietveld Refinement of XRD Data

sample	lattice parameters					$S(MO_2)$ (Å)[a]	$I(LiO_2)$ (Å)
	a (Å)	c (Å)	c/a	V(Å³)	z		
E5	2.8676(3)	14.199(1)	4.9515	101.11(2)	0.2578(1)	2.145	2.588
E10	2.8638(3)	14.190(1)	4.9550	100.79(2)	0.2574(2)	2.155	2.575
E15	2.8607(3)	14.183(1)	4.9579	100.51(2)	0.2573(1)	2.157	2.571

[a]M = transition metal (Ni, Co, Mn); slab thickness: $S(MO_2) = 2[(1/3) - z]c$; interslab space thickness: $I(LiO_2) = (c/3) - S(MO_2)$.
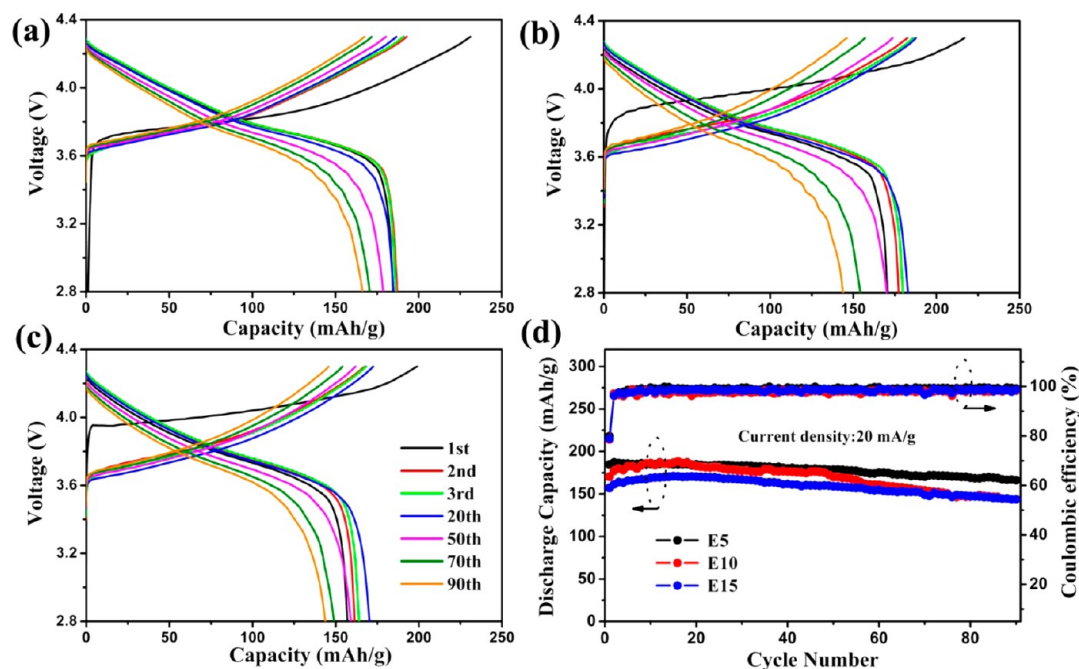

Figure 6. Charge−discharge curves of different cycles for samples (a) E5, (b) E10, and (c) E15 at a current density of 20 mA/g in a voltage window of 2.8−4.3 V at room temperature. (d) Corresponding cycling performance at a current density of 20 mA/g in a voltage window of 2.8−4.3 V for samples E5, E10, and E15.

cobalt ions for all samples are in an oxidation state of +3 with a low-spin state.[24,25] Figure 5b₁−b₃ shows the XPS spectra for Mn 2p, in which two broad main peaks were observed at about 642.2 and 653.7 eV with FWHM >3 eV. Both peaks are ascribed to Mn 2p$_{3/2}$ and 2p$_{1/2}$. The binding energy difference between 2p$_{3/2}$ and 2p$_{1/2}$ are 11.5 eV, which indicates that Mn ions are present in +4.[26,27] The broadened FWHM observed are due to the overlapping of photoelectron peak and Auger peaks of Ni.[28] Figure 5c₁−c₃ shows Ni 2p XPS data for samples E5, E10, and E15. With increasing the amount of excess lithium source from 5 to 15 mol %, the most intense peaks attributed to Ni 2p$_{3/2}$ shifted from lower binding energy of 855.1 to 855.6 eV, suggesting that the amount of Ni³⁺ in samples E5, E10, and E15 are progressively increased. Further, when using mixed Gaussian−Lorentzian profiles as previously reported for LiNi$_{0.7}$Co$_{0.15}$Co$_{0.15}$O$_2$ material,[29,30] Ni 2p$_{3/2}$ peaks are well fitted in two subsignals at 854.39 eV for Ni²⁺ and at 855.52 eV for Ni³⁺ with FWHM of 1.56 and 2.7 eV, respectively. From the fitting results, one can see that the relative content of Ni³⁺ varies from 74.1 to 91.7 mol % in a sequence: E5 < E10 < E15, which is consistent with our XRD refinement results. A redox titration method, using KMnO₄ solution as the titrant, has been performed to further confirm the valence states of the transition metals in the bulk structure. The results showed that the amounts of Ni³⁺ were 75(3)% for E5, 87(2)% for E10, and 93(1)% for E15, which are all consistent with those calculated

by XPS data analyses. In short, the rationality of XRD refinements is confirmed by XPS data and redox titration.

In addition, the calculated lattice parameters represented by a and c are listed in Table 2. "a" parameter is a measure of interlayer metal−metal distance and "c" value is the sum of MO$_6$ octahedron layer thickness (slab thickness: $S(MO_2)$) and LiO$_6$ octahedron layer thickness (interslab space thickness: $I(LiO_2)$) in the layer structure of LiMO$_2$.[18,31] With increasing the lithium-excess content from 5 to 15 mol %, both parameters of a and c decrease, whereas the ratios of c/a increase, accompanying with the increase of slab thickness and the decrease of interslab space thickness. These results can be explained according to the relevant ionic radii (Li⁺, 0.76 Å; Ni²⁺, 0.69 Å; Ni³⁺, 0.56 Å; Co³⁺, 0.63 Å; and Mn⁴⁺, 0.54 Å).[11,18] On the one hand, Ni²⁺ with smaller radius occupies at Li layer would result in the decrease of $I(LiO_2)$. On the other hand, location of Li⁺ with a largest radius in transition metal layer would increase the slab thickness of $S(MO_2)$. The decrease in c axis from E5 to E15 indicates a dominance of the decrease in $I(LiO_2)$ over the increase in $S(MO_2)$. The decrease in interslab space thickness ($I(LiO_2)$) does not favor the processes of lithium ion's intercalation and deintercalation, but leading to the deterioration of electrochemical performance. Therefore, it can be expected that samples E10 and E15 may have relatively poorer electrochemical performance than sample E5.

3.2. Impacts of Lithium Content on Electrochemical Performance of LiNi$_{0.7}$Co$_{0.15}$Mn$_{0.15}$O$_2$ Microspheres. Elec-

trochemical performance of the samples E5, E10, and E15 sintered with different amounts of lithium source (Li-excess of 5, 10, and 15 mol %, respectively) were tested by configuring them as the laboratory-based CR2025 coin half-cell employing Li metal as the anode. Figure 6a−c compares the charge−discharge curves of different cycles at a current density of 20 mA/g in a voltage range from 2.8 to 4.3 V at room temperature. The initial discharge capacity decreased from 184.7 mAh/g for E5 to 157.0 mAh/g for E15 with increasing the amount of lithium source, accompanying with an increase in charging voltage platform from ca. 3.7 to 3.9 V. Combined with Figure 6d, it can be seen that sample E5 has the highest discharge capacities and best cycling capability among all samples. The discharge capacity of 90th cycle is 166.2 mAh/g for sample E5, which is higher than 143.8 mAh/g for both samples E10 and E15. The capacity retention ratio relative to the highest discharge capacity among the 90 cycles is 88.8, 76.9, and 84% for samples E5, E10, and E15, respectively. Moreover, an increase of capacity in the initial stage (1−20th cycle) was observed for samples E10 and E15, rather than sample E5. These indicate that (i) sample E5 with a fewer amount of Li^+/Ni^{2+} disordered arrangement exhibits a better electrochemical performance; and (ii) samples E10 and E15 need an electrochemical activation process, which may derive from more amounts of Li^+/Ni^{2+} disordered arrangement in them. In addition, for sample E10, the discharge capacity declines rapidly after 50th cycle. This should be attributed to the largest number of Ni^{2+} ions in Li layer (3b site), i.e., the lithium/nickel disordering occupation not only decreases the discharge capacity but also impedes Li^+ ionic diffusivity.[10,19]

Differential capacity (dQ/dV) profiles could help us to better understand the influence of the lithium/nickel ions disordering occupation on the redox behaviors of samples. As shown in Figure 7, at a current density of 20 mA/g, sample E5 showed redox peaks at around 3.78 V on first charging, and at 3.63 and 3.75 V on first discharging, whereas samples E10 and E15 exhibited two redox peaks at around 3.95 and 4.12 V on first charging. The big difference observed in the redox peaks at the first cycle of samples E5, E10, and E15 should be related to the difference of Li^+/Ni^{2+} disorder arrangements. During the subsequent cycles, two distinct redox peaks at 3.65 and 3.75 V appeared on charging process, which are due to the phase transitions of hexagonal to monoclinic (H1 → M) for these three samples.[32] As the cycling proceeded, the redox peaks for sample E5 are more stable than that of samples E10 and E15, resulting in the good cycle performance for sample E5. In addition, for sample E10 (Figure 7b), the oxidation and reduction peaks in regions I and II that are ascribed to monoclinic phase (inactivated phase) become dominated, which may be the main reason for the deterioration of cycling performance. Furthermore, another reason that explains the poor cycle capability of sample E10 is an increase in internal resistance indicated by the increase in initial discharge voltage drop, as shown in region III.

The cycle performances of the samples E5, E10, and E15 at high current densities of 50, 100, 200, and 400 mA/g in a voltage window of 2.8−4.3 V at room temperature were also measured, as shown in Figure 8. At the same current density of 50 mA/g, the initial discharge capacities were 171.1, 161.5, and 147.4 mAh/g for sample E5, E10, and E15, respectively. After 100 cycles, the discharge capacities were 150.0, 142.3, and 134.6 mAh/g, whereas the corresponding capacity retention ratios to the highest discharge capacities among 100 cycles were
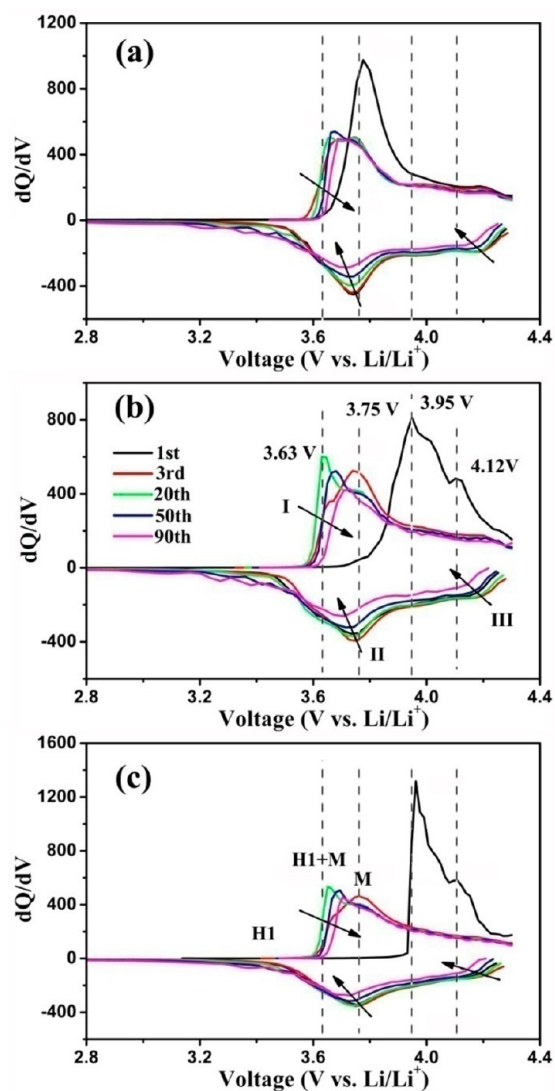

Figure 7. Differential capacity vs voltage curves of different cycles at a current density of 20 mA/g for samples: (a) E5, (b) E10, and (c) E15.

86.8, 82.0, and 83.8%, respectively. When the current densities increased to 100 mA/g, the discharge capacities after 100 cycles were 136.7, 129.5, 116.5 mAh/g, and their capacity retention ratios were 86.0, 84.0, and 78.3% for sample E5, E10, and E15, respectively. Moreover, there are increases in capacity at the initial stage (1−20th cycle) for samples E10 and E15, but not for sample E5, which can be understood as mentioned above. Obviously, sample E5 with a fewer amount of Li^+/Ni^{2+} disordering exhibits capacity and cycle capabilities superior to those for samples E10 and E15 with larger amounts of Li^+/Ni^{2+} disordering at smaller current density. When the current densities further increased to 200 and 400 mA/g, although all samples showed the relatively poor cycle performances with capacity retention ratios of <80%, sample E5 still exhibited discharge capacities larger than samples E10 and E15 in initial stage of cycle. Comparing to the initial discharge curves of all samples at different current densities of 50, 100, 200, and 400 mA/g, respectively, as shown in Figure 8a, c, and e, sample E5 had a best rate performance and a largest initial discharge capacity at different rates, whereas sample E10 showed the largest discharge voltage drop at bigger current densities, indicating sample E10 had a larger internal resistance. The best
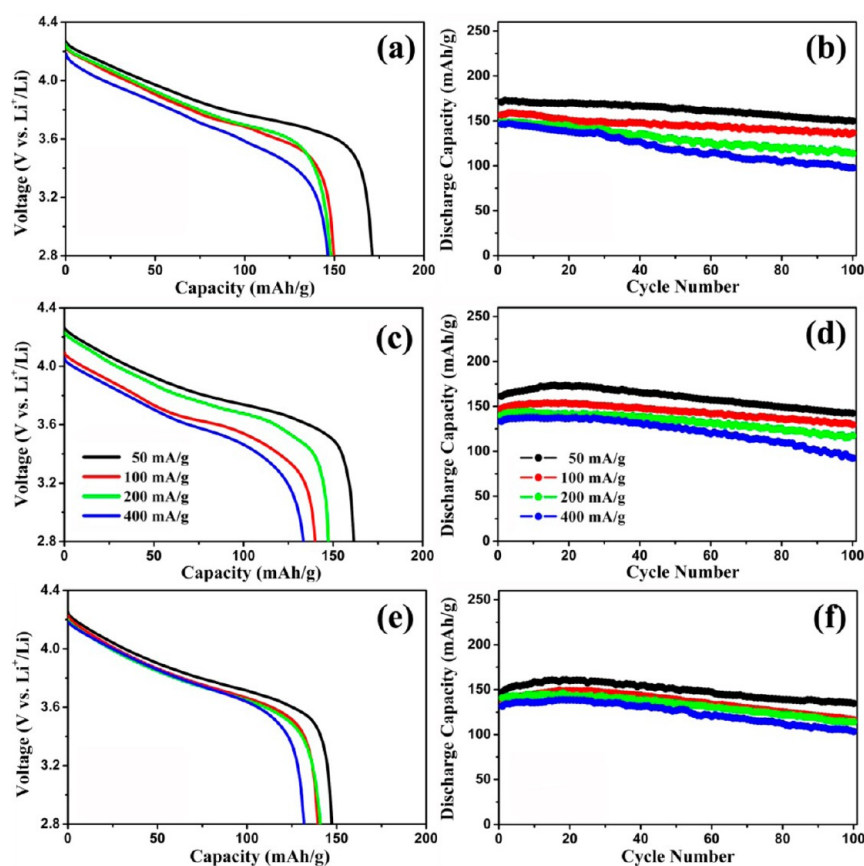
Figure 8. Rate and cycling performance at current densities of 50, 100, 200, and 400 mA/g in a voltage window of 2.8−4.3 V at room temperature for the samples (a, b) E5, (c, d) E10, and (e, f) E15.
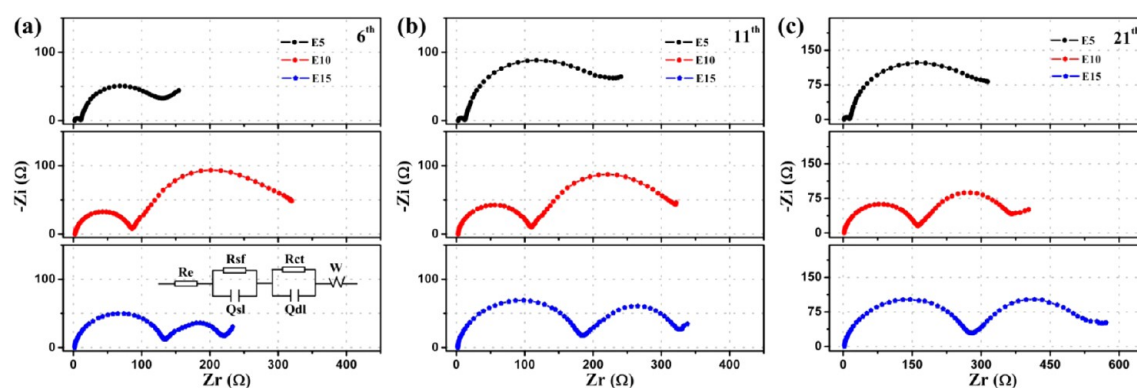

Figure 9. Electrochemical impedance spectroscopy of different cells for samples E5, E10, and E15 measured when charged to 4.3 V with a current density of 20 mA/g at given cycles: (a) 6th cycle, (b) 11th cycle, and (c) 21th cycle. Inset in a is the equivalent circuit diagram.

electrochemical performance observed for sample E5 should be due to the least amount of Li^+/Ni^{2+} disordered arrangement and the largest interslab space thickness.

Electrochemical impedance spectroscopy (EIS) is an important technique for evaluating the interfacial electro-chemistry as well as the reaction kinetics in lithium ion battery materials.[33−37] Impedance spectra were measured on the $LiNi_{0.7}Co_{0.15}Mn_{0.15}O_2$/Li cells to further understand the difference of electrochemical performance for samples E5, E10, and E15 with different extents of Li^+/Ni^{2+} disordered arrangement. Nyquist plots were obtained in the frequency range from 100 kHz to 10 mHz at fully charged state after 6, 11, and 21 cycles at a current density of 20 mA/g, in which Z_i and

Z_r denote the imaginary and real part of impedances, respectively. The impedance spectra were analyzed by Zswinpwin software, and the data fitted to the equivalent electrical circuit is shown in inset of Figure 9a. Here, R_e represents the internal resistance of the cell derived from the electrolyte and current collector. R_{sf} and Q_{sl} are the resistance and capacitance of the SEI film, the formation of which involves a series of spontaneous reactions between the cathode active materials and the electrolyte solvents. R_{ct} and Q_{dl} are the charge transfer resistance due to the lithium intercalation/deinterca-lation process and double layer capacitance, and W describes the Warburg impedance which is directly related to the solid state diffusion of lithium ion inside the active particles, signified

by the straight sloping line at the low-frequency region.[26] The Warburg impedance is not shown for some impedance spectra because of the limit of test frequency.

As shown in Figure 9, all Niquist plots exhibited two semicircles in the high and middle frequency regions. The values of R_e, R_{sf}, and R_{ct} obtained after different cycles are listed in Table S4−6 (Supporting Information). It can be seen that there are no significant changes for the values of R_{sf} from sixth to 21th cycles for sample E5, which indicates that SEI films are stable in the cycle process. As the same cycles from sixth to 21th, however, the values of R_{sf} for sample E10 increase from 80.9 to 153.8 Ω, and for sample E15, it increases from 123.9 to 256.6 Ω, leading to the lower discharge capacities for samples E10 and E15. The reason for the growth of SEI films may be related to the enhanced reactions between lithium ions and electrolyte, because the smaller interslab space thickness like that of 2.575 Å for E10 and 2.571 Å for E15 makes Li$^+$ ions difficult to be reinserted back to the interslab. In addition, the values of R_{total} (R_e+ R_{sf}+ R_{ct}) for all samples increased with the cycles going on, which results in a decrease in discharge capacity.

4. CONCLUSION

Nickel-rich layered LiNi$_{0.7}$Co$_{0.15}$Mn$_{0.15}$O$_2$ microspheres with different extents of Li$^+$/Ni^{2+} ion disordering were successfully synthesized by sintering the mixtures of Ni−Co−Mn-based spherical precursors and different amounts of lithium source. With increasing the content of lithium source, the amount of Li$^+$ ions at the 3a site of transition metal layer increases, which leads to an increase in the amount of Ni^{3+} ions in LiNi$_{0.7}$Co$_{0.15}$Mn$_{0.15}$O$_2$ materials. As a result, there occurred decreases in lattice parameters, a, c, and interslab space thickness of unit cell. Li$^+$/Ni^{2+} disordering also alters the electrochemical performance of all samples. The sample with Li-excess of 5 mol % exhibited a best electrochemical performance, which is related to its least amount of Li$^+$/Ni^{2+} disordered arrangement and the largest interslab space thickness. The methodology and the relevant results reported herein for nickel-rich layered LiNi$_{0.7}$Co$_{0.15}$Mn$_{0.15}$O$_2$ microspheres may provide hints for obtaining other nickel-rich layered metal oxide microspherical materials with superior electrochemical performance.

■ ASSOCIATED CONTENT

Ⓢ Supporting Information
Rietveld refinement on atomic coordinates, and parameters fitted for EIS data of different cycles of all samples. This material is available free of charge via the Internet at http://pubs.acs.org/.

■ AUTHOR INFORMATION

Corresponding Author
*E-mail: lipingli@fjirsm.ac.cn. Fax: (+) 86-591-83702122.

Notes
The authors declare no competing financial interest.

■ ACKNOWLEDGMENTS

■ REFERENCES

(1) Tarascon, J. M.; Armand, M. Issues and Challenges Facing Rechargeable Lithium Batteries. *Nature* **2001**, *414*, 359−367.

(2) Kang, K.; Meng, Y. S.; Bréger, J.; Grey, C. P.; Ceder, G. Electrodes with High Power and High Capacity for Rechargeable Lithium Batteries. *Science* **2006**, *311*, 977−980.

(3) Guo, Y.-G.; Hu, J.-S.; Wan, L.-J. Nanostructured Materials for Electrochemical Energy Conversion and Storage Devices. *Adv. Mater.* **2008**, *20*, 2878−2887.

(4) Manthiram, A.; Vadivel Murugan, A.; Sarkar, A.; Muraliganth, T. Nanostructured Electrode Materials for Electrochemical Energy Storage and Cconversion. *Energy Environ. Sci.* **2008**, *1*, 621−638.

(5) Goodenough, J. B.; Kim, Y. Challenges for Rechargeable Li Batteries. *Chem. Mater.* **2009**, *22*, 587−603.

(6) Xu, X.; Lee, S.; Jeong, S.; Kim, Y.; Cho, J. Recent Progress on Nanostructured 4 V Cathode Materials for Li-ion Batteries for Mobile Electronics. *Mater. Today* **2013**, *16*, 487−495.

(7) Reimers, J. N.; Dahn, J. R. Electrochemical and In-Situ X-Ray Diffraction Studies of Lithium Intercalation in Li$_x$CoO$_2$. *J. Electrochem. Soc.* **1992**, *139*, 2091−2097.

(8) Ohzuku, T.; Ueda, A. Solid-State Redox Reactions of LiCoO$_2$ ($R\overline{3}m$) for 4 V Secondary Lithium Cells. *J. Electrochem. Soc.* **1994**, *141*, 2972−2977.

(9) Luo, D.; Li, G.; Yu, C.; Yang, L.; Zheng, J.; Guan, X.; Li, L. Low-concentration Donor-doped LiCoO$_2$ as a High Performance Cathode Material for Li-Ion Batteries to Operate between −10.4 and 45.4 °C. *J. Mater. Chem.* **2012**, *22*, 22233−22241.

(10) Kraytsberg, A.; Ein-Eli, Y. Higher, Stronger, Better—A Review of 5 V Cathode Materials for Advanced Lithium-Ion Batteries. *Adv. Energy Mater.* **2012**, *2*, 922−939.

(11) Ellis, B. L.; Lee, K. T.; Nazar, L. F. Positive Electrode Materials for Li-Ion and Li-Batteries. *Chem. Mater.* **2010**, *22*, 691−714.

(12) Kalyani, P.; Kalaiselvi, N. Various Aspects of LiNiO$_2$ Chemistry: A review. *Sci. Technol. Adv. Mater.* **2005**, *6*, 689−703.

(13) Winter, M.; Besenhard, J. O.; Spahr, M. E.; Novák, P. Insertion Electrode Materials for Rechargeable Lithium Batteries. *Adv. Mater.* **1998**, *10*, 725−763.

(14) Koyama, Y.; Arai, H.; Tanaka, I.; Uchimoto, Y.; Ogumi, Z. Defect Chemistry in Layered LiMO$_2$ (M = Co, Ni, Mn, and Li$_{1/3}$Mn$_{2/3}$) by First-Principles Calculations. *Chem. Mater.* **2012**, *24*, 3886−3894.

(15) Hoang, K.; Johannes, M. D. Defect Chemistry in Layered Transition-Metal Oxides from Screened Hybrid Density Functional Calculations. *J. Mater. Chem. A* **2014**, *2*, 5224−5235.

(16) Chen, H.; Dawson, J. A.; Harding, J. H. Effects of Cationic Substitution on Structural Defects in Layered Cathode Materials LiNiO$_2$. *J.Mater. Chem. A* **2014**, *2*, 7988−7996.

(17) Jo, M.; Noh, M.; Oh, P.; Kim, Y.; Cho, J. A New High Power LiNi$_{0.81}$Co$_{0.1}$Al$_{0.09}$O$_2$ Cathode Material for Lithium-Ion Batteries. *Adv. Energy Mater.* **2014**, DOI: 10.1002/aenm.201301583.

(18) Sun, Y. K.; Lee, D. J.; Lee, Y. J.; Chen, Z.; Myung, S. T. Cobalt-Free Nickel Rich Layered Oxide Cathodes for Lithium-Ion Batteries. *ACS Appl. Mater. Interfaces* **2013**, *5*, 11434−11440.

(19) Yu, H.; Qian, Y.; Otani, M.; Tang, D.; Guo, S.; Zhu, Y.; Zhou, H. Study of the Lithium/Nickel Ions Exchange in the Layered LiNi$_{0.42}$Mn$_{0.42}$Co$_{0.16}$O$_2$ Cathode Material for Lithium Ion Batteries: Experimental and First-Principles Calculations. *Energy Environ. Sci.* **2014**, *7*, 1068−1078.

(20) Fu, C.; Li, G.; Luo, D.; Huang, X.; Zheng, J.; Li, L. One-Step Calcination-Free Synthesis of Multicomponent Spinel Assembled Microspheres for High-Performance Anodes of Li-Ion Batteries: A Case Study of MnCo$_2$O$_4$. *ACS Appl. Mater. Interfaces* **2014**, *6*, 2439−2449.

(21) Toby, B. H. EXPGUI, a Graphical User Interface for GSAS. *J. Appl. Crystallogr.* **2001**, *34*, 210−213.

(22) Guo, X.-J.; Li, Y.-X.; Zheng, M.; Zheng, J.-M.; Li, J.; Gong, Z.-L.; Yang, Y. Structural and Electrochemical Characterization of xLi-[Li$_{1/3}$Mn$_{2/3}$]O$_2$·(1−x)Li[Ni$_{1/3}$Mn$_{1/3}$Co$_{1/3}$]O$_2$ (0 ≤ x ≤ 0.9) as

Cathode Materials for Lithium Ion Batteries. *J. Power Sources* **2008**, *184*, 414−419.

(23) Shi, S. J.; Tu, J. P.; Tang, Y. Y.; Zhang, Y. Q.; Liu, X. Y.; Wang, X. L.; Gu, C. D. Enhanced Electrochemical Performance of LiF-Modified $LiNi_{1/3}Co_{1/3}Mn_{1/3}O_2$ Cathode Materials for Li-Ion Batteries. *J. Power Sources* **2013**, *225*, 338−346.

(24) Yu, C.; Guan, X.; Li, G.; Zheng, J.; Li, L. A Novel Approach to Composite Electrode $0.3Li_2MnO_3-0.7LiMn_{1/3}Ni_{1/3}Co_{1/3}O_2$ in Lithium-Ion Batteries with an Anomalous Capacity and Cycling Stability at 45.4°C. *Scripta Mater.* **2012**, *66*, 300−303.

(25) Munakata, F.; Takahashi, H.; Akimune, Y.; Shichi, Y.; Tanimura, M.; Inoue, Y.; Itti, R.; Koyama, Y. Electronic State and Valence Control of $LaCoO_3$: Difference between La-Deficient and Sr-Substituting Effects. *Phys. Rev. B* **1997**, *56*, 979−982.

(26) Luo, D.; Li, G.; Guan, X.; Yu, C.; Zheng, J.; Zhang, X.; Li, L. Novel Synthesis of $Li_{1.2}Mn_{0.4}Co_{0.4}O_2$ that Shows an Excellent Electrochemical Performance from −10.4 to 45.4 °C. *J. Mater. Chem. A* **2013**, *1*, 1220−1227.

(27) Zhang, X.; Luo, D.; Li, G.; Zheng, J.; Yu, C.; Guan, X.; Fu, C.; Huang, X.; Li, L. Self-Adjusted Oxygen-Partial-Pressure Approach to the Improved Electrochemical Performance of Electrode $Li[Li_{0.14}Mn_{0.47}Ni_{0.25}Co_{0.14}]O_2$ for Lithium-Ion Batteries. *J. Mater. Chem. A* **2013**, *1*, 9721−9729.

(28) Kosova, N. V.; Devyatkina, E. T.; Kaichev, V. V. Optimization of Ni^{2+}/Ni^{3+} Ratio in Layered $Li(Ni,Mn,Co)O_2$ Cathodes for Better Electrochemistry. *J. Power Sources* **2007**, *174*, 965−969.

(29) Sun, Y.-K.; Myung, S.-T.; Park, B.-C.; Prakash, J.; Belharouak, I.; Amine, K. High-Energy Cathode Material for Long-Life and Safe Lithium Batteries. *Nat. Mater.* **2009**, *8*, 320−324.

(30) Cho, Y.; Lee, S.; Lee, Y.; Hong, T.; Cho, J. Spinel-Layered Core-Shell Cathode Materials for Li-Ion Batteries. *Adv. Energy Mater.* **2011**, *1*, 821−828.

(31) Guilmard, M.; Rougier, A.; Grüne, M.; Croguennec, L.; Delmas, C. Effects of Aluminum on the Structural and Electrochemical Properties of $LiNiO_2$. *J. Power Sources* **2003**, *115*, 305−314.

(32) Noh, H.-J.; Youn, S.; Yoon, C. S.; Sun, Y.-K. Comparison of the Structural and Electrochemical Properties of Layered $Li[Ni_xCo_yMn_z]O_2$ (x = 1/3, 0.5, 0.6, 0.7, 0.8, and 0.85) Cathode Material for Lithium-Ion Batteries. *J. Power Sources* **2013**, *233*, 121−130.

(33) Luo, D.; Li, G.; Fu, C.; Zheng, J.; Fan, J.; Li, Q.; Li, L. A New Spinel-Layered Li-Rich Microsphere as a High-Rate Cathode Material for Li-Ion Batteries. *Adv. Energy Mater.* **2014**, DOI: 10.1002/aenm.201400062.

(34) Fu, C.; Li, G.; Luo, D.; Zheng, J.; Li, L. Gel-Combustion Synthesis of $Li_{1.2}Mn_{0.4}Co_{0.4}O_2$ Composites with a High Capacity and Superior Rate Capability for Lithium-Ion Batteries. *J. Mater. Chem. A* **2014**, *2*, 1471−1483.

(35) Zhou, Y.; Wang, J.; Hu, Y.; O'Hayre, R.; Shao, Z. A Porous $LiFePO_4$ and Carbon Nanotube Composite. *Chem. Commun.* **2010**, *46*, 7151−7153.

(36) Zhao, B.; Yu, X.; Cai, R.; Ran, R.; Wang, H.; Shao, Z. Solution Combustion Synthesis of High-Rate Performance Carbon-Coated Lithium Iron Phosphate from Inexpensive Iron (III) Raw Material. *J. Mater. Chem.* **2012**, *22*, 2900−2907.

(37) Li, Q.; Li, G.; Fu, C.; Luo, D.; Fan, J.; Li, L. K^+-Doped $Li_{1.2}Mn_{0.54}Co_{0.13}Ni_{0.13}O_2$: A Novel Cathode Material with an Enhanced Cycling Stability for Lithium-Ion Batteries. *ACS Appl. Mater. Interfaces* **2014**, *6*, 10330−10341.